PAPER

Check for updates

Optical nonlinearity of Gd-doped VSe₂ nanoflowers for photonic device applications†

Abinash Parida,[a] Banaja Dandasena,[a] Tapas Kumar Mallik,[b] Sripan Chinnaiyah[c] and Ramakanta Naik [ID] *[a]

The nonlinear optical characteristics of semiconductor nanoparticles play an important role in optoelectronic devices. In this regard, we study the linear and nonlinear optical properties, along with the electrical, structural, and morphological properties of Gd-doped VSe₂ nanoflowers. Herein, we successfully synthesized $V_{1-x}Gd_xSe_2$ (x = 0, 0.1, 0.2, and 0.3) nanoflowers using a simple hydrothermal technique. Structural analysis shows the pure VSe₂ phase and peak shifting due to the doping of Gd. The prepared samples show a nano flower-like morphology, which is uniformly distributed throughout the sample. EDX analysis confirms all the constituents and doped elements in the prepared samples. In the optical analysis, the Kubelka–Munk equation is used to calculate the bandgap values, which show high bandgap values of 2.6–3.6 eV for the prepared samples. The electrical measurement shows a higher conducting ability for the VSe₂ sample. The nonlinear optical Z-scan investigation showed that the RSA behavior and peak-valley pattern had negative n_2 values, indicating a self-defocusing effect. Here, VSe₂ exhibits better nonlinear properties. The third-order nonlinear optical NLO susceptibility $\chi^{(3)}$ values indicate that the VSe₂ material could be used for future NLO applications.

1. Introduction

Two-dimensional materials with various layered architectures are known as transition metal dichalcogenides (TMDs). These structures remain intact by interlayer van der Waals (vdW) interactions and strong intralayer ionic covalent connections. Because of their varied crystalline phases and chemical compositions, TMDs exhibit a range of electrical characteristics, such as semiconducting, metallic, and semi-metallic behaviors. Numerous opportunities for better efficiency of nanoscale electronic gadgets have been presented by these compounds. TMDs exhibiting semiconductor properties include materials such as MoS₂, MoSe₂, and WSe₂, with bandgaps between 0.4 and 2.3 eV.[1] The electrical and optical properties of these band formations can be altered by applying mechanical strain or external electric fields. This makes them attractive options for creating ultrathin field-effect transistors with very high

performance.[2] Vanadium-based compounds can undergo multiple phases, each with distinct electrical and structural properties. Vanadium oxides and selenides exhibit strong anisotropic behavior and optical characteristics that change notably based on their phase and structure. The compounds of vanadium have strong interactions with light that increase the ability of the photodetector to absorb light, thus enhancing its capability.[3] However, VSe₂, another metallic member of the TMD group, exhibits a strong light interaction. Though the system as a whole displays paramagnetism, individual layers exhibit ferromagnetism even at ambient temperature.[4] The low-temperature charge density wave (CDW) order in VSe₂ is noteworthy. At 10^6 Sm⁻¹,[5] its conductivity is exceptionally high. These characteristics make it a suitable material for electronic gadgets and spinning.[6]

The qualities of VSe₂, such as electron transport-related characteristics and high conductivity, could enable the development of independent, low-power, fast-responding photodetectors. Broadband photodetectors are in high demand in various fields, including multispectral detection, optical communications, imaging, and sensing.[7,8] Nonetheless, the spectrum response ranges of commercial semiconductor materials are still limited, and they frequently face issues such as low operating temperatures, complicated fabrication techniques, and high production prices.[9,10] Two-dimensional materials, notably 2H-phase TMDs, can address these difficulties owing to their unique optical[11,12] and electrical properties.[13–15] VSe₂ possesses outstanding linear optical

[a] Department of Engineering and Materials Physics, Institute of Chemical Technology-IndianOil Odisha Campus, Bhubaneswar, 751013, India. E-mail: ramakanta.naik@gmail.com

[b] Department of Physics, Utkal University, Vani Vihar, 751004, India

[c] Department of Physics, Dayananda Sagar Academy of Technology and Management, Udayapura, Bangalore, 560082, India

properties, which are principally due to its typical layered structure and metallic crystal phase.[16] Its crystalline structure allows for great light absorption and transmission, making it an ideal contender for various optical applications. The large surface area of VSe_2 facilitates improved light–matter interactions, resulting in remarkable optical reactions. The capacity of a material to have tunable optical properties enhances its utility by allowing alterations in its optical features based on external stimuli such as temperature and applied electric fields. In addition to its linear optical performance, VSe_2 exhibits interesting nonlinear optical features that are essential for laser technology and optical data processing.[17] The nonlinear optical response of VSe_2 is governed by its electronic band structure, which enables two-photon absorption and third-harmonic generation.[18,19] This makes VSe_2 an ideal material for creating novel photonic devices because it can efficiently transfer frequencies and generate harmonic signals through nonlinear interactions.[20,21] Recently, there have been several studies regarding nonlinear properties[22] and their relative applications in various fields, such as photonics,[23,24] modulator,[25] fiber laser, and IR applications.[26] Gadolinium (Gd) doping of metal chalcogenides is an important area of research that focuses on improving the optical characteristics of materials for various applications. Specific investigations on Gd-doped VSe_2 are rare, and insights can be gained from research on similar materials. The optical and electrical properties of VSe_2 may be altered by the addition of Gd, which can be used in different applications.[27] According to previous studies, adding Gd to materials such as bismuth vanadate ($BiVO_4$) increases the mobility of charge carriers. Gd doping causes lattice distortions that promote charge transport, which is responsible for this improvement.[28] It has been demonstrated that doping VSe_2 with substances such as reduced graphene oxide improves ultrafast third-order nonlinear optical responses, which are essential for all-optical data processing and optical switching applications.[18] This implies that Gd doping may also improve the nonlinear optical characteristics of VSe_2, enabling its use in sophisticated photonic applications.

Doping transition metal dichalcogenides (TMDs) with different elements to improve their characteristics has been investigated in recent studies. Gd^{3+}-doped WS_2 nanoflakes have demonstrated promise in cancer theranostics by providing combined photothermal and radiation therapy as well as multimodal imaging.[29] The functionalization of TMDs with metallic nanoparticles, especially MoS_2, has shown promise for gas sensing applications and notable doping effects.[30] The ability to manipulate magnetic and optical properties has been demonstrated by first-principles studies of lanthanide substitutional doping in MoS_2 monolayers. Gd, Eu, and Tm dopants have been shown to induce significant magnetization and refine optical responses.[31] These developments in TMD doping have created new opportunities for a range of fields, such as biomedicine, electronics, and optoelectronics. Optical investigations have shown that Gd doping has a considerable effect on the photoluminescence (PL) properties of ZnO. As Gd concentrations grow, the intensity ratio of visible emissions grows, indicating an increase in oxygen vacancies. As Gd concentration increases, the band gap energy decreases from 3.31 to 3.23 eV, indicating that Gd influences the electrical structure of ZnO.[32] This makes Gd-doped ZnO an attractive choice for optoelectronic applications notably because of its improved photocatalytic characteristics.[32] The increased optical characteristics of Gd-doped metal chalcogenide make it suitable for a wide range of optoelectronic applications. Researchers have identified possible applications in sensors, LEDs, and photovoltaics. Specifically, Gd-doped ZnO has been found to increase the effectiveness of photocatalytic reactions, which are critical for environmental remediation.[32,33] Furthermore, the distinctive optical reactions caused by Gd doping open up new possibilities in domains such as UV sterilization and biological detection.[34] To determine their use in optoelectronics and different applications, it is crucial to investigate optical nonlinearities in nanostructured semiconductor materials.

Here, we synthesize pure VSe_2 and Gd-doped VSe_2 samples. Examining innovative compounds, such as $VGdSe_2$, expands our basic knowledge of materials science and improves the various materials available for optoelectronic applications. Our current study used the hydrothermal process to demonstrate a simple one-pot synthesis methodology for the Gd-doped VSe_2 material. This method allowed us to successfully prepare the Gd-doped VSe_2 composition using a simple and easy way. Several characterizations were used to investigate the nature of the sample. X-ray diffraction (XRD) was utilized to study the material's phase and crystallinity formation. Morphological analysis was performed using a field emission scanning electron microscope (FESEM) and transmission electron microscopy (TEM). To explore the structural properties, pictures were acquired using high-resolution transmission electron microscopy (HRTEM) and selected area electron diffraction (SAED). UV-visible spectroscopy was used to measure reflectance data, which made it easier to calculate the optical bandgap value.

2. Experimental

2.1. Chemicals and materials

We used ammonium metavanadate (NH_4VO_3, 98%, Fisher Scientific), gadolinium(III) nitrate hexahydrate [Gd$(NO_3)_3$·$6H_2O$] (99%, Sigma Aldrich), oxalic acid ($C_2H_2O_4$·$2H_2O$), and selenium powder (99%, Alfa Aesar) as the vanadium, gadolinium, and selenium, sources, respectively, to prepare the samples.

2.2. Synthesis method

Here, samples were prepared using the conventional hydrothermal method, with the sources of vanadium, gadolinium, and selenium being NH_4VO_3, [Gd$(NO_3)_3$·$6H_2O$], and selenium powder, respectively. A common hydrothermal method was used to produce flower-like VSe_2. First, 40 ml of DI water was taken in a beaker with the stochiometric amounts of 1 mmol of NH_4VO_3, 2 mmol of Se powder, and 9.5 mmol of $C_2H_2O_4$·$2H_2O$ and then mixed in the beaker. To prepare the solution, it was subjected to stirring for 1 h. After that, the solution was kept in a 50 ml autoclave, and the autoclave was placed in a hot air oven at 200 °C for 24 h. After that, the synthesized product was
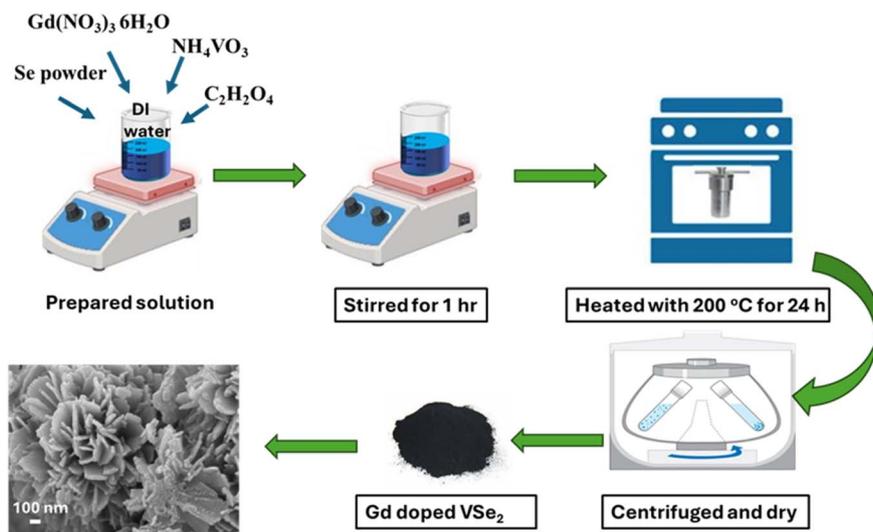
Fig. 1 Preparation method of $V_{1-x}Gd_xSe_2$ samples using the hydrothermal technique.

washed three times in DI water and ethanol; then, the collected precipitate was dried in a vacuum at 60 °C for 24 h. The same hydrothermal synthesis method was then used three times to dope Gd (0.1, 0.2, and 0.3 mmol). The corresponding samples were called VS (pure VSe_2), GVS-1 (Gd doped 0.1 mmol), GVS-2 (Gd doped 0.2 mmol), and GVS-3 (Gd doped 0.3 mmol) throughout this paper. After that, the sample was collected. A schematic diagram of the synthesis procedure is depicted in Fig. 1.

2.3. Characterization

Multiple processes are utilized to examine the morphological, optical, and structural changes in the prepared sample. A Bruker D8 Advance diffractometer was used for the XRD measurements. During the measurements, an incident beam of Cu K_α ($\lambda = 1.54$ Å) operating at 30 kV and 40 mA was used, spanning an angular range of 10°–70°. Raman measurements were taken by utilizing RENISHAW in *Via* Raman Microscopy (Model-RE 04). Using TEM (JEOL, TEM-2100 Plus) and FESEM (JEOL, JSM-7601FPLUS), the sample's surface morphology was investigated. Energy-dispersive X-ray spectroscopy (EDX) measurements were performed to analyze the elemental composition of the samples. The reflectance data in the wavelength range of 250–800 nm were taken by applying a UV-Vis-NIR spectrophotometer (JASCO-660). The Z-Scan measurements technique is used to conduct NLO analyses of the samples. A Z-Scan system (Model-HO-ED-LOE-03) from HOLMARC is used to perform the Z-scan measurement. It has a 150 mm linear translation stage with a step size of 0.1 mm and a 100 mW 532 nm (diode-pumped solid-state) DPSS continuous-wave (CW) laser source. Samples with a sufficient sample length of 1 mm are prepared as films on glass surfaces using the drop-cast technique. The open aperture (OA) and close aperture (CA) Z-scan measurements were carried out parallelly using a linearly polarized 532 nm laser beam.

3. Results and discussion

3.1. XRD and Raman analysis

The XRD study of the material provides detailed insight into its structural properties. Fig. 2(a) illustrates the XRD patterns of the as-prepared VSe_2 and Gd-doped VSe_2. The XRD pattern shows eight significant peaks. It could be readily indexed to the standard (JCPDS card no: 01-89-1641) corresponding to VSe_2. The reflection peaks localized at 14.6°, 29.2°, 30.8°, 34.1°, 42.8°, 54.6°, 60.7° and 66.09° corresponding to (0 0 1), (0 0 2), (1 0 0), (0 1 1), (1 0 2), (1 1 0), (0 0 4), and (2 0 1) planes, respectively.[35] Fig. S1 of the ESI† shows that the peaks shifted to lower angles after doping gadolinium (Gd). This might be due to the larger ionic radius of Gd compared to vanadium (V) or selenium (Se), which are constituent elements of VSe_2.[36] When Gd is incorporated into the VSe_2 crystal structure, the atomic size mismatch can cause local lattice distortions. This leads to a change in the interatomic spacing, which results in a shift in the XRD peaks.[36] In this case, the peak shifts to lower angles, and doping leads to the expansion of the lattice and increases the interplanar spacing (*d*-spacing).

Raman spectroscopy was used to analyze the structural alterations in the prepared samples. A spectroscopic study in the 100–500 cm^{-1} range was performed at room temperature, as illustrated in Fig. 2(b). The Raman spectra make it easier to understand the vibrations linked to changes in polarizability and the resulting changes in molecule structure. They also provide information about chemical bonding and atomic configurations. There are three measure peaks found at 140, 280, and 405 cm^{-1}. The vibration modes of E_{1g} and A_{1g} can be attributed to VSe_2 at 310 and 435 cm^{-1}, respectively.[37,38] The Raman spectra of the prepared composite clearly display the VSe_2 Raman bands. The bands at 280 and 405 cm^{-1}, respectively, reflect the E_{2g} and A_{1g} vibration modes of VSe_2, respectively.[39,40] According to Najafi *et al.*, the E_{2g} and A_{1g} bands of 1T-VSe_2 are responsible for the two peaks in the bulk VSe_2 observed
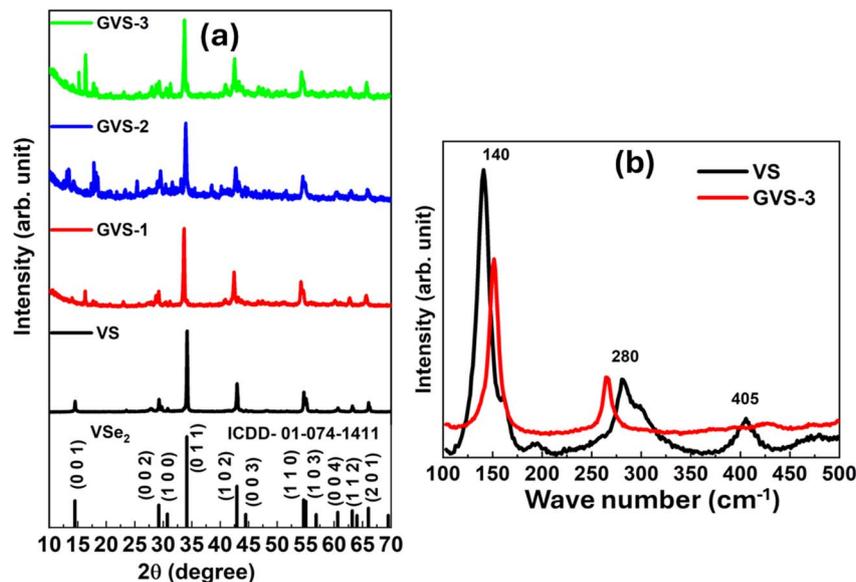
Fig. 2 (a) XRD pattern and (b) Raman spectra of VS and GVS samples.

at 140 and 210 cm^{-1}, respectively.[41,42] The peak at 140 cm^{-1} shifted towards the higher wavenumber for the GVS-3 sample owing to the Gd doping.

3.2. FESEM, EDX, and TEM analyses

The variation in morphology in the nanocomposite produced with varying vanadium and gadolinium levels can be observed in the FESEM study. The morphology of pure VSe$_2$ is shown in Fig. 3. Fig. 3(a) demonstrates that the hydrothermally synthesized VSe$_2$ produces several flower-like structures. A structure resembling a flower is created by the accumulation of thin sheets. The structure of marigold flowers is comparable to that of microflowers. The prepared samples show nanoflower-like morphology, which is again accumulated to form micro sphere-like shapes in the range of 1.7–2.5 μm that uniformly spread throughout the sample. Fig. 3(b) depicts the micrometer view of the prepared pure VS sample. These FESEM images of the sample are taken within two different magnifications, which are at 100 nm scale and 1 μm scale, which shows that the particle is in a nano sphere-like structure.

Fig. 4 shows the magnified images of the Gd-doped samples, and the micrometer view images of the Gd-doped samples are presented in Fig. S2 of the ESI file.† The thickness of the thin sheets is calculated using ImageJ software. We observe that the thickness increases with the Gd doping from 26.9 nm, 32.4 nm, and 33.3 nm to 35.4 nm for VS, GVS1, GVS2, and GVS3, respectively. Fig. 5 illustrates the EDX spectra of the prepared composition, showing the existence of constituent elements in the material. The VS sample is a pure VSe$_2$ composition with elemental composition V and Se in the EDX spectra, while the doped samples show the Gd peak in the EDX spectra. The elemental mapping images of all the constituent elements of the GVS-3 sample are presented in Fig. S3 of the ESI.†

The particle size and crystalline behavior can be understood with the help of HR-TEM and SAED studies. As shown in Fig. 6(a), the TEM image of the VS sample displays nanosheets organized as flowers. The HRTEM pictures are used to calculate the lattice spacing value, and Fig. 6(b) shows the corresponding lattice plane. The spacing value is found to be approximately 0.3 and 0.26 nm, respectively, representing the (0 0 2) and (0 1 1) lattice planes. These outcomes are consistent with the prepared
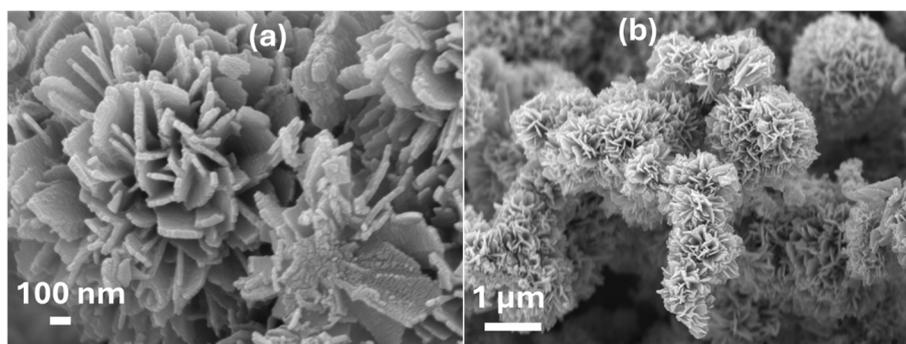

Fig. 3 FESEM image of pure VSe$_2$ sample: (a) nanometer scale and (b) micrometer scale.
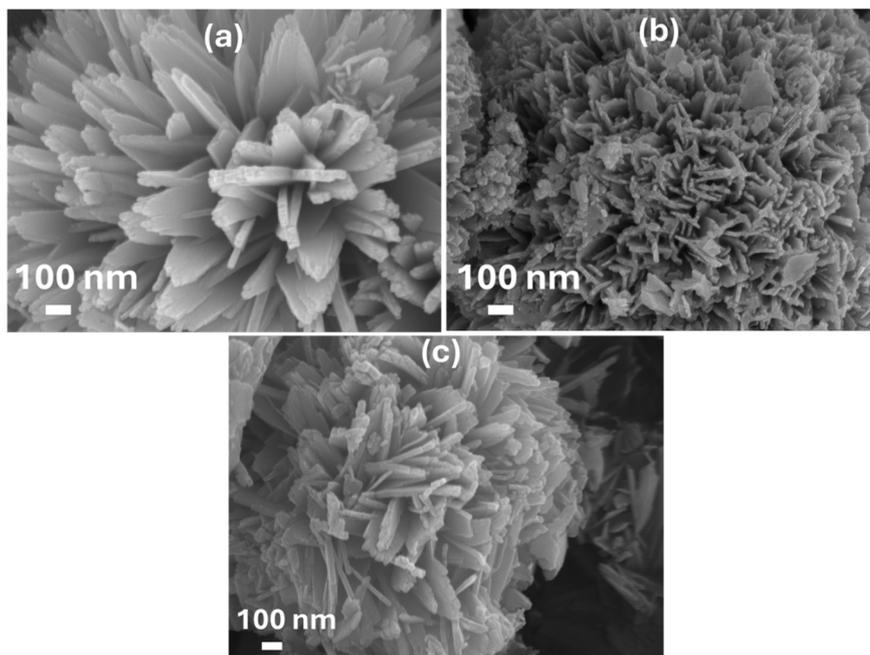
Fig. 4   FESEM images of (a) GVS-1, (b) GVS-2, and (c) GVS-3 at a nanometer scale.
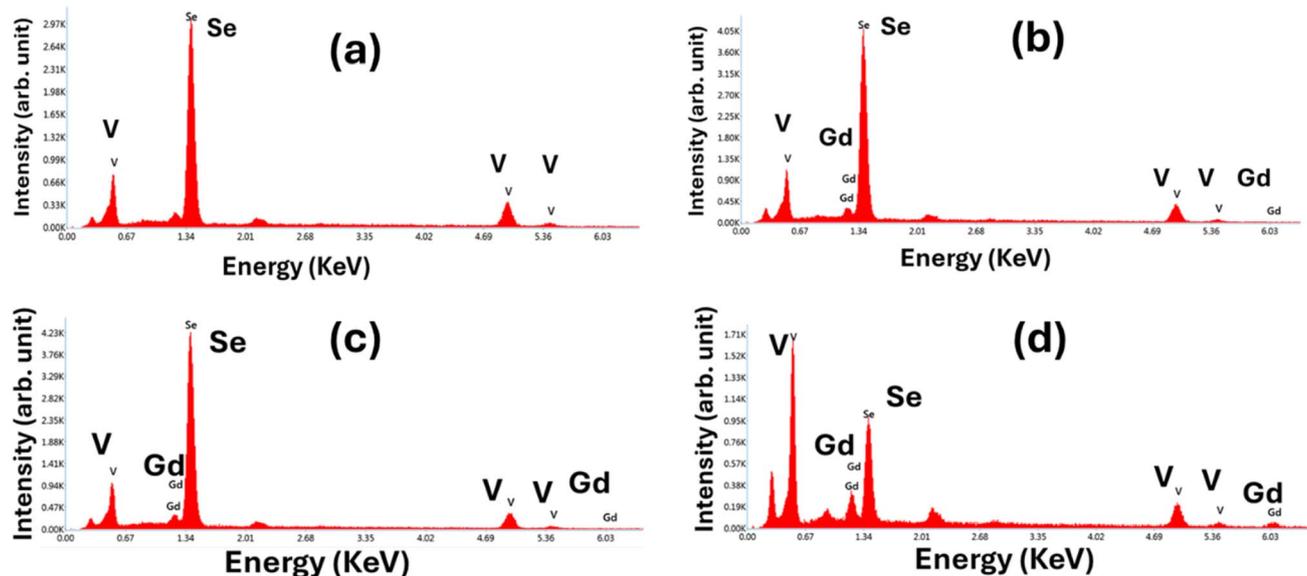

Fig. 5   EDX spectra of (a) VS, (b) GVS-1, (c) GVS-2, and (d) GVS-3 samples.

sample's XRD data. The sample's crystallinity is represented by the SAED patterns, as depicted in Fig. 6(c). The SAED image has certain ring patterns made up of bright spots that help determine the crystalline properties. Overall, the structural study, which includes SAED, HRTEM, and XRD, demonstrates that all of the findings are in agreement and consistent.

3.3.   Optical analysis

The synthesized VS and GVS sample's optical reflectance spectra at wavelengths ranging from 250 to 800 nm are shown in

Fig. 7(a). In semiconductor materials, the energy difference between an electron's high and low energy levels is enhanced as it shifts from valence to the conduction band. The basic absorption edge shifts toward low wavelengths as the sample's Gd doping rises. With increasing Gd doping, the intensity of the reflectance spectra rises, reaching its maximum for the GVS-3 sample. The Kubelka–Munk approach was used to evaluate the band gap value of the material.[43] The Kubelka–Munk theory can apply to this situation. This equation can be expressed as follows:[44]
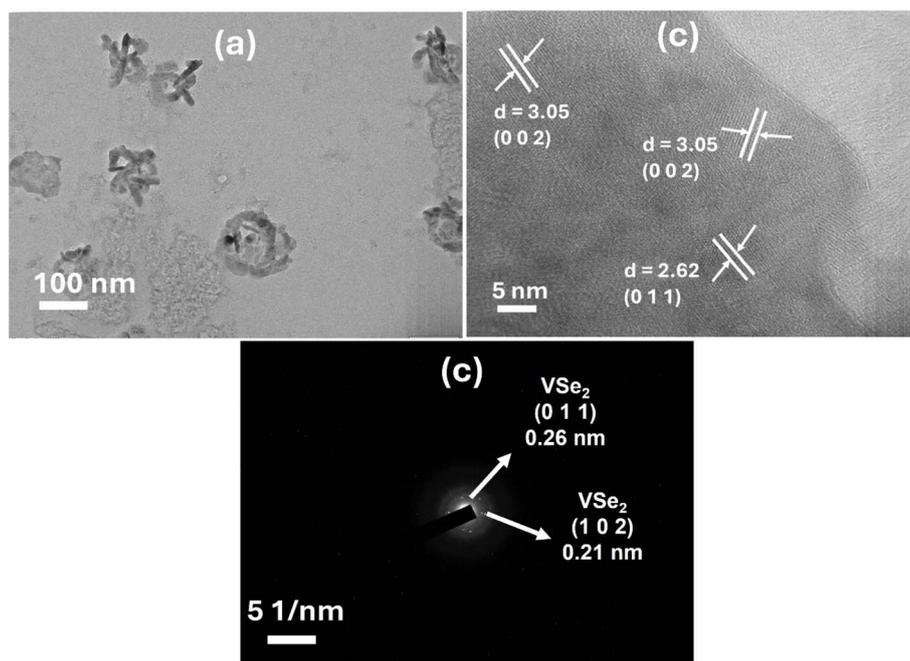
Fig. 6 (a) TEM image of the GVS-3 samples, (b) HRTEM image, and (c) SAED pattern of the GVS-3 sample.

$$\frac{K}{S} = \frac{(1 - R_\infty)^2}{2R_\infty} \equiv F(R_\infty), \qquad (1)$$

where $F(R)$ is known as the Kubelka–Munk function and R_∞ is the diffuse reflectance. The absorption coefficient is associated with the Tauc relation and the optical band gap values E_g. The relationship can be stated as follows:[7]

$$\alpha h\nu = A(h\nu - E_g)^m \qquad (2)$$

where A is the proportionality constant, ν is the light frequency, and α is the absorption coefficient. To determine the direct band gap for the crystalline materials, the value of "m" is assumed to be 1/2. Absorption 'K' is equal to 2α when the incoming light is subject to perfect diffuse scattering. The scattering coefficient 'S' is regarded as constant in this instance. Consequently, the $F(R)$ and the absorption coefficient "K" are proportional. According to the theory of Kubelka and Munk presented in 1931, reflectance spectra can be transformed into corresponding absorption spectra by applying the Kubelka–Munk function ($F(R_\infty)$):

$$F(R_\infty) = \frac{K}{S} = \frac{(1 - R_\infty)}{2R_\infty},$$

where 'K' denotes the absorption coefficient and S denotes the scattering coefficient.[43] K and S depend on the intrinsic absorption 'α' and scattering 's' coefficients of the material such that $\frac{\alpha}{s} \propto \frac{K}{S}$. The definition of $F(R_\infty)$ involves the K–M coefficients (K and S) to avoid possible confusion with the α and s coefficients.

Eqn (2) allows us to obtain the following equation:

$$[F(R_\infty)h\nu]^2 = A(h\nu - E_g). \qquad (3)$$

The bandgap of the synthesized material can be assessed by plotting the $(F(R_\infty)h\nu)^2$ vs. $h\nu$. Fig. 7(b–e) shows the calculated bandgaps of the prepared samples. The composition with a larger Gd doping concentration has a larger bandgap than the undoped VSe_2 sample. Table 1 displays the calculated bandgap values. According to the calculation, the bandgap value of VS is 2.6 eV, and for the GVS-3 sample, it increases to 3.6 eV as the Gd doping amount rises. The increase in the band gap after doping Gd on VSe_2 can be attributed to the complex interplay between charge carrier localization, modification of the Fermi level, spin–orbit coupling, and charges in the electronics structure owing to the presence of a dopant (Gd).[45] Each of these factors can contribute to widening the electronic gap between the valence and conduction bands in the doped material.[46]

We reported similar results in our previous work, where the samples with Mo doping in VSe_2 show higher bandgap values.[47] Yi et al. reported that the high bandgap values and the values increased with the Gd doping concentration.[45] Variations in bandgap values were also found using the Kubelka Munk function for the calculation.[48] Optical and electrical parameters of semiconducting materials can be understood by refractive index parameters. This attribute, along with the optical bandgap, characterizes the possible usage of compounds in the production of electronic devices. Generally, compounds with a shorter bandgap and a larger refractive index offer a wide range of applications, including detectors, solar cells, and waveguides. A useful method for determining the refractive index of the current sample is to use the Dimitrov and Sakka formula. As given below, this entails adding the optical bandgap data to the Dimitrov and Sakka equation below:[49]
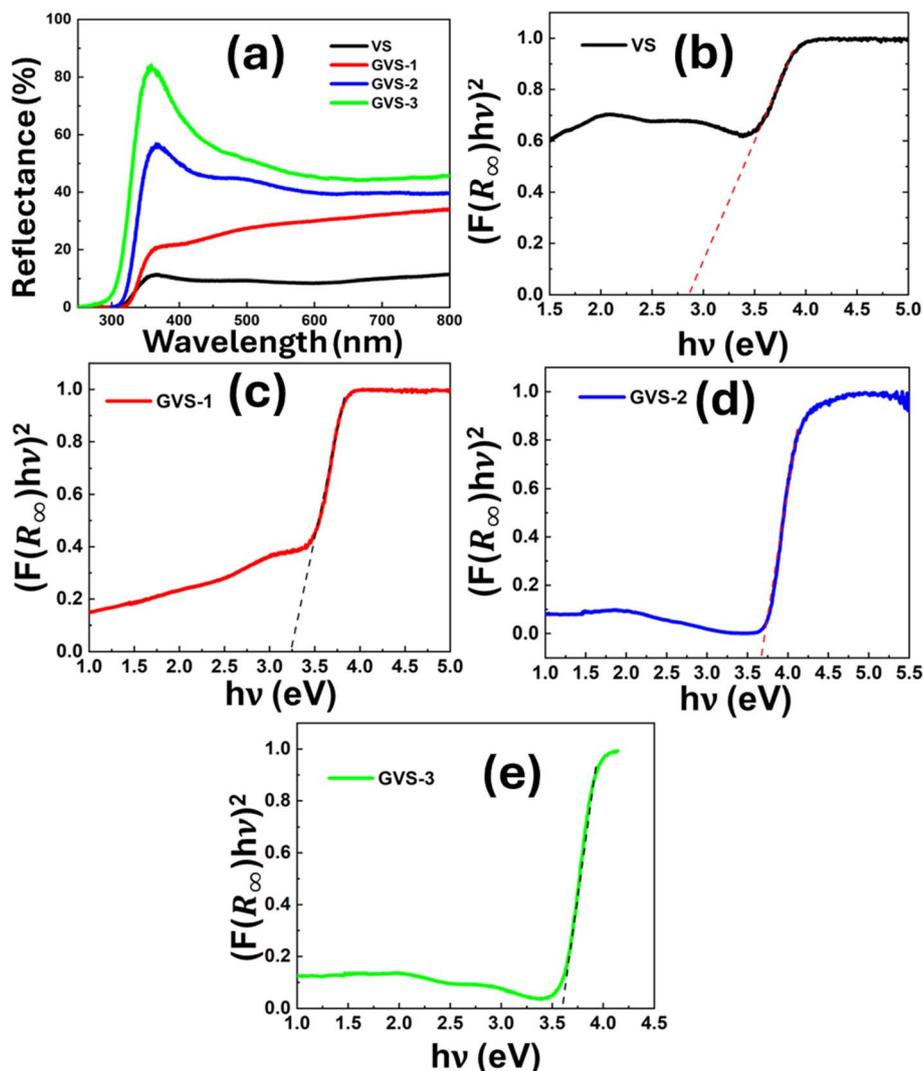
Fig. 7 (a) Reflectance curve of $V_{1-x}Gd_xSe_2$ samples, (b) bandgap of VS, (c) bandgap of GVS-1, (d) bandgap of GVS-2, and (e) bandgap of GVS-3 sample.

Table 1 Optical parameters of the VS and GVS samples

Estimated optical parameters	VS	GVS-1	GVS-2	GVS-3
Direct optical bandgap (E_g) (eV)	2.62	3.13	3.6	3.69
Refractive index (n)	2.50	2.36	2.25	2.23
Dielectric constant (ε)	6.28	5.58	5.07	4.98

$$\frac{n^2 - 1}{n^2 + 1} = 1 - \left(\frac{E_g}{20}\right)^{\frac{1}{2}}. \tag{4}$$

The refractive index (n) values are given in Table 1. The dielectric constant, which is the ratio of a substance's permittivity to that of free space, shows how well a material can concentrate electric flux. Furthermore, the equation ($\varepsilon = n^2$) can be used to obtain the dielectric constant using the refractive index (n). The obtained values of 'n' and 'ε' are shown in Table 1. It is discovered that the bandgap values exhibit opposing behaviour for both n and 'ε' values. Shkir *et al.* reported a variation of refractive index in the range of 1.87–3.81 and similar dielectric constant values that change with Gd doping concentration.[50] Similar values of refractive index and dielectric constant have been reported for different compounds that are used for application in optoelectronic devices, optical TCE, and photo electrocatalytic devices in the future.[51,52]

3.4. XPS study

The XPS study aims to examine the oxidation states of the components in the present samples. XPS is a surface science technique that can be used to determine the elemental composition and binding states of a material's surface. Here, a GVS-3 sample was used for the XPS analysis. This investigation aims to examine variations in the element's core-level energies. Fig. 8 shows the XPS spectra of V-2p, Gd-3d, and Se-3d. The survey scan shown in Fig. 8(a) depicts the existence of each compositional element. The standardization of elemental peaks

was based on the carbon peak at 285 eV. The produced nano-material has two notable peaks, V $2p_{3/2}$ and V $2p_{1/2}$, at binding energies of 517 and 524.5 eV, respectively, as shown in Fig. 8(b). The presence of the V^{4+} of vanadium is indicated by a peak at about 517 eV.[53] Fig. 8(c) shows that the Gd peaks at 143 and 148.7 eV are attributed to the +3 oxidation state.[54] Additionally, the XPS analysis of Se 3d is shown in Fig. 8(d). Selenium's −2 oxidation state is responsible for the distinct two peaks in the spectra: Se $3d_{5/2}$ at 55 eV and Se $3d_{3/2}$ at 56.3 eV.[55] These outcomes demonstrate that the GVS composite samples were successfully synthesized.

The reference $V2p_{3/2}$ binding energies of the V^{0+}, V^{2+}, V^{3+}, V^{4+}, and V^{5+} states of vanadium oxides are almost equivalent to 511∼512 eV, 512∼513 eV, 515.7–8 eV, 516 eV, and 516.6–517.7 eV, respectively. The +4-valance state of the VSe_2 sample is represented by the $V2p_{3/2}$ state observed at 517 eV. Similar findings for vanadium 2p have also been reported by Vijaya-kumar et al.[56]

3.5. Electrical study

To evaluate the capability of compounds to be used in opto-electronic devices, their electrical characteristics were investigated. The I–V test was carried out at ambient temperature with a DC voltage that was scanned from −10 to 10 V. The characteristics plot of the prepared samples is shown in Fig. 9. The linear and symmetrical I–V curves show their ohmic characteristics. The ohmic properties are indicated by the symmetric and linear I–V curves. The figure indicates that the electrical

characteristics of the samples are good. The electrical behaviour of the sample decreases with increasing Gd doping. Higher resistance and lower current are found in the sample with a higher concentration of Gd. The GVS-3 sample has a low current of about 4 nA; however, the compound VS displays a higher current of about 17 μA. The GVS-2 sample has a current of about 130 nA, which is very low compared to the VS sample. Therefore, in the comparative IV plot, both GVS-2 and GVS-3 seem to overlap, as shown in Fig. 9. Similar findings from our earlier research, where VSe_2 exhibits superior electrical properties over the doped samples, were also discovered.[47] Fig. S4 of the ESI file† displays the individual I–V curves for the light and dark currents for each sample. For comparative analysis, all the I–V plots of each sample in light and dark modes are shown. The
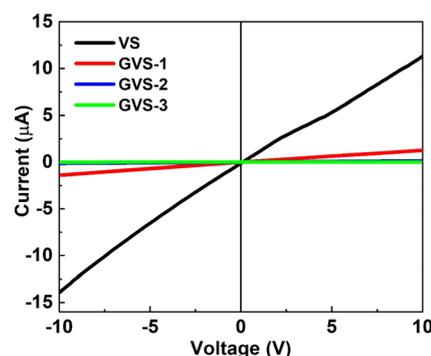

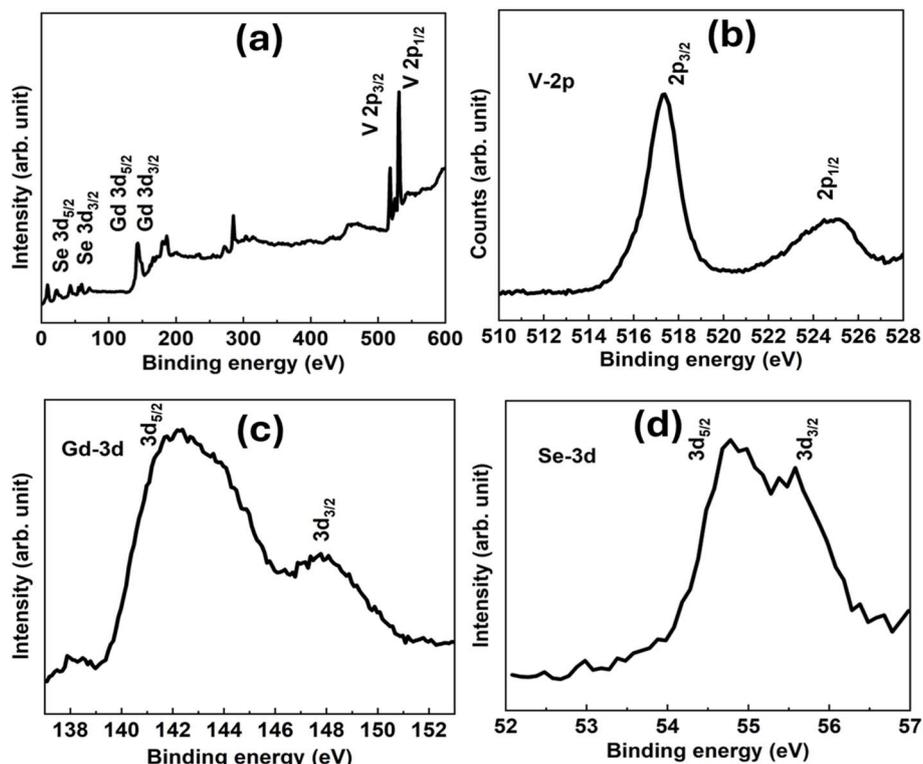Fig. 9 I–V characteristics of VS and GVS samples.

Fig. 8 XPS spectra of (a) GVS-3, (b) V 2p, (c) Gd 3d, and (d) Se 3d of GVS-3 samples.

GVS-3 sample with the highest doping shows the lowest current of about 4 nA among the prepared samples. Subsequently, the GVS-3 sample did not show a photo response; therefore, the light and dark current overlapped, as shown in Fig. S4(d).† It is clear from this that the light current is always higher than the dark current.[57] This increase in photocurrent in comparison to the dark current is caused by the separation of charges and light and matter interactions.

3.6. Z-scan study

The Z-scan method is used to measure the absorption coefficient (β), refractive index (n_2), and third-order NLO susceptibility ($\chi^{(3)}$). This study helps to understand the optical nonlinearity of the VS and GVS samples.

3.6.1 Open aperture (OA) – nonlinear absorption. The nonlinear absorption parameters associated with saturable absorption are investigated using the OA Z-scan data. The data for OA are measured directly at photodetector-1 (PD1), while the data for CA are measured at photodetector-2 (PD2) with an aperture. Reverse saturation absorption (RSA) and saturable absorption (SA) can be distinguished at the focal point by observing their nature. The RSA appears as a valley, whereas the SA appears as a peak at $Z = 0$. Negative refraction takes place in the opposite peak-valley configuration ($n_2 < 0$), while positive refraction arises in the case of valley-peak configuration ($n_2 > 0$).[58]

The OA graphs depicted in Fig. 10(b and d) show the RSA behavior of the VS and GVS-3 samples. Following

normalization, the OA results are fitted using the transmittance formula below based on the material's nonlinear absorption characteristic:[59]

$$T(Z) = 1 - \frac{\beta I_0 L_{\text{eff}}}{\left(1 + \dfrac{Z^2}{Z_R{}^2}\right)2\sqrt{2}}, \tag{5}$$

where L_{eff} is the film's effective length, $T(Z)$ is the normalized transmittance, I_0 is the beam intensity at focus, and Z_R is the Rayleigh range. The L_{eff} can be determined using the following formula: $L_{\text{eff}} = (1 - e^{-\alpha L})/\alpha$, where α and L denote the absorption coefficient and thickness of the sample, respectively. It is observed that the transmittance value decreases near the focal point, and the valley declines at increasing intensities, indicating induced absorption in thin films, according to the OA results. According to the calculations, the β values for the VS and GVS-3 samples are around 0.848 and 0.392 cm W^{-1}, respectively. The VS sample was found to have the highest β value with intrinsic RSA. Pure VSe$_2$ exhibits greater β values and intrinsic RSA likely owing to its unaltered electronic structure, allowing for effective nonlinear absorption processes. Doping with Gd causes alterations that may impair these processes, resulting in reduced nonlinear optical responses. As we also found in the electrical study, the sample's electrical behavior decreases with increasing Gd doping. Research on VSe$_2$ hybridized with CoSe$_2$ nanoparticles shows higher third-order nonlinear optical responses owing to increased charge transfer states enabled by metal ions.[60]
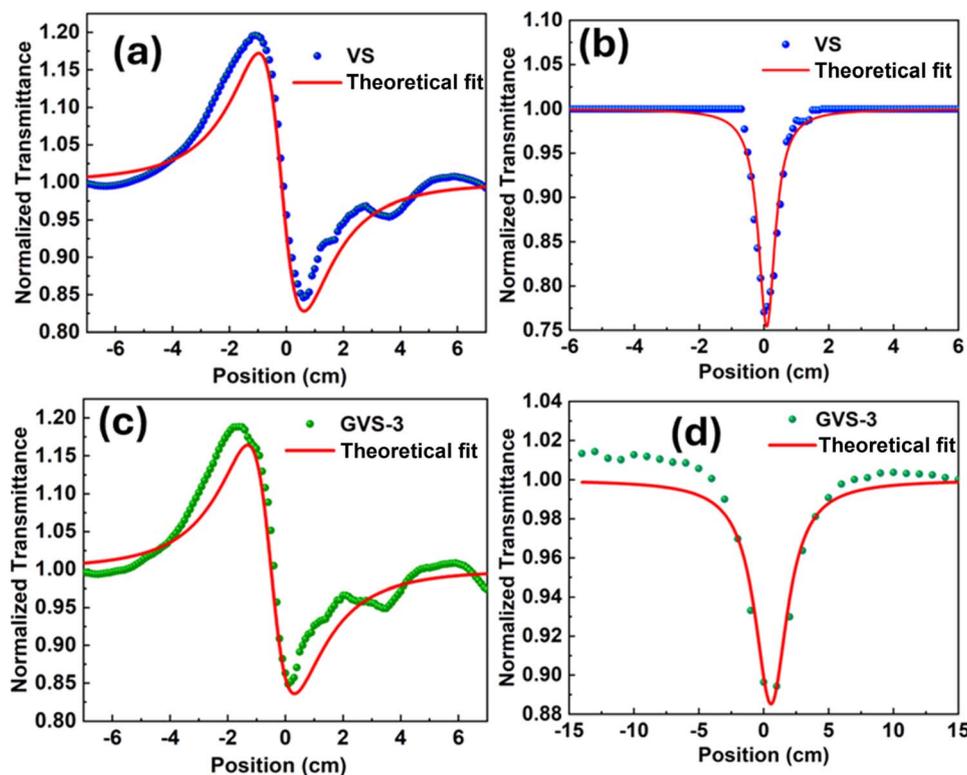

Fig. 10 (a and c) CA Z-Scan fitting and (b and d) OA Z-Scan fitting of the VS and GVS-3 samples, respectively.

Table 2 Parameters found in the Z-scan analysis

Samples	β (cm W^{-1})	$n_2 \times 10^{-6}$ (cm^2 W^{-1})	$\chi_R^{(3)} \times 10^{-2}$ (e.s.u)	$\chi_{Im}^{(3)} \times 10^{-2}$ (e.s.u)	$\chi^{(3)} \times 10^{-2}$ (e.s.u)
VS	0.848	8.668	13.749	57.03	58.664
GVS-3	0.392	8.187	10.332	20.994	23.399

3.6.2 Closed aperture – nonlinear refraction (NLR). The CA mode helps to examine the nonlinear refraction response of the VS and GVS-3 compositions, as depicted in Fig. 10(a and c). The pre-focal transmittance maximum (peak) signature is followed by a post-focal transmittance minimum (valley) in the CA Z-scan curves for both films. It is evident from the curve's structure that this peak-valley configuration suggests a negative phase shift of n_2, confirming the self-defocus tendency of the sample. The nonlinear refraction characteristic of the material yields the following equation, which fits the CA results:[59]

$$T(Z) = 1 - \frac{4 \times \dfrac{Z}{Z_R} \times \Delta\varphi}{\left(1 + \dfrac{Z^2}{Z_R^2}\right)\left(9 + \dfrac{Z^2}{Z_R^2}\right)}, \quad (6)$$

where the nonlinearly induced phase shift is denoted by $\Delta\Phi$.

The value of n_2 is evaluated by the following equation:

$$n_2 = \frac{\lambda \Delta\Phi_0}{2\pi I_0 L_{eff}}, \quad (7)$$

where λ is the wavelength of the incoming laser beam. The evaluated n_2 values of the VS and GVS-3 samples are 8.66×10^{-6} cm^2 W^{-1} and 8.01×10^{-6} cm^2 W^{-1}, respectively. In intensity-dependent focusing response, the VS sample had a maximum n_2 value. Here, it is evident that as the amount of Gd doping increases, the n_2 values for the GVS-3 samples decrease. These materials are thoroughly examined to determine the precise cause of this event. As we have discussed above, doping with Gd causes alterations that may impair these processes, resulting in reduced nonlinear optical responses. Therefore, the nonlinear refractive index also decreases for the GVS samples. From the linear optical analysis, we also found that the bandgap increases and the refractive index decreases with the Gd doping.

The following equations link the real and imaginary components of third-order NLO susceptibility $\chi^{(3)}$ to n_2 and β:[61]

$$\text{Re } \chi^{(3)}(\text{esu}) = \frac{10^{-4} \varepsilon_0 C^2 n_0^2}{\pi} n_2 (\text{cm}^2 \text{ W}^{-1}), \quad (8)$$

$$\text{Im } \chi^{(3)}(\text{esu}) = \frac{10^{-2} \varepsilon_0 C^2 n_0^2 \lambda}{4\pi^2} \beta (\text{cm W}^{-1}), \quad (9)$$

where ε_0 represents the electrical permittivity of free space with a value of 8.85×10^{-14} F cm^{-1}, n_0 is the linear refractive index, and c is the light velocity in a vacuum.

The electronic polarizability of a substance is shown by its nonlinear susceptibility. The third-order nonlinear susceptibility $|\chi^{(3)}|$ is evaluated by utilizing the real and imaginary $\chi^{(3)}$ value. The equation given below describes the nonlinear susceptibility of a material showing simultaneous nonlinear refraction and nonlinear absorption:[62]

$$|\chi^{(3)}| = [(\text{Re}[\chi^{(3)}])^2 + (\text{Im}[\chi^{(3)}])^2]^{1/2} \text{ (esu)} \quad (10)$$

The nonlinear results found from the Z-scan experiment, such as β, n_2, and $\chi^{(3)}$ values, are presented in Table 2. All the samples had positive NLO parameter values, with the VS sample having higher overall values than the GVS-3 sample. This material property may be used in various optoelectronic devices, such as modulating devices and optical switching.

There are various factors affecting the physical-based nonlinearity such as 2 PA, thermal effect, and nonlinear scattering effect. According to theory, 2 PA requires band gaps in the 2.65–2.78 eV range, where $E_g/2 \leq h\upsilon \leq E_g$.[63] In this instance, the energy of the incoming beam, or "$h\upsilon$," is 2.33 eV. The 2 PA process can be regarded as the cause of the nonlinearity because the prepared samples satisfy the necessary requirements. Every sample has an Im $\chi^{(3)}$ higher than Re $\chi^{(3)}$, indicating that the compound reacts in an absorptive way rather than a refractive way to incident light. When employing a CW laser, the Im $\chi^{(3)}$ works better than the Re $\chi^{(3)}$ because of nonlinear interactions, a strong absorption nature, and thermal effects from continuous energy input. Continuous use of a CW laser may cause localized heating of the material, where every particle acts as a heating center.[61] This heating alters the material's electronic structure by populating higher vibrational states that absorb lighter. The optical properties are altered by high temperature, increasing absorption and raising the imaginary part of susceptibility. This creates a feedback loop in which the higher temperature boosts absorption and solidifies the dominance of the imaginary component.

4. Conclusion

In conclusion, VSe$_2$ and Gd-doped VSe$_2$ samples were synthesized utilizing a simple hydrothermal process. This is a low-cost, simple approach for making such compounds in bulk, with numerous benefits. The crystallographic study reveals that the prepared samples are crystalline and have a pure VSe$_2$ phase. The XRD peaks shifted towards the lower angle owing to the Gd doping. Raman analysis also shows similar structural information, where Raman peaks shifted towards higher wave numbers with doping. XPS analysis confirmed the presence of Gd content in the V$_{1-x}$Gd$_x$Se$_2$ samples with a proper oxidation state. The optical analysis shows that the prepared samples have high bandgap values ranging from 2.6 to 3.6 eV, and these values increase as the Gd doping amount increases. The prepared samples show a nanoflower-like morphology, which

agglomerates to form micro sphere-like shapes that are uniformly spread throughout the sample. The *I–V* characteristics of the VSe$_2$ sample were found to be better than those of the doped samples, showing a maximum current of around 17 μA. The nonlinear investigation showed that the RSA behaviour and peak-valley pattern had negative n_2 values, indicating a self-defocusing effect. The two-photon absorption process controls the material's NLO characteristics. Here, VSe$_2$ shows better nonlinear properties. Future NLO applications may employ VSe$_2$ material owing to its higher nonlinear values. No studies, such as those on optical and nonlinear responses related to the Gd-doped VSe$_2$ compound, have been reported. Therefore, in the present study, we attempted to explore the optical, electrical, and nonlinear responses of the compound. Although the pure VSe$_2$ samples show better nonlinear responses, the Gd-doped sample shows higher bandgap values. Therefore, GVS samples with high-bandgap values can be used in photovoltaic applications.

Data availability

The data supporting this article are included in the ESI.† The data are plotted using Origin software. Analysis and quantification of images were performed using ImageJ software.

Conflicts of interest

There are no conflicts of interest to declare.

Acknowledgements

References

1 N. Zibouche, P. Philipsen, T. Heine and A. Kuc, *Phys. Chem. Chem. Phys.*, 2014, **16**, 11251–11255.

2 J. B. Khurgin, *Opt.*, 2015, **2**, 740–742.

3 J. Li, L. Jiang, W. Ma, T. Wu, Q. Qiu, Y. Shi, W. Zhou, N. Yao and Z. Huang, *ACS Appl. Nano Mater.*, 2022, **5**, 5158–5167.

4 K. Xu, P. Chen, X. Li, C. Wu, Y. Guo, J. Zhao, X. Wu and Y. Xie, *Angew. Chem.*, 2013, **125**, 10671.

5 G. Duvjir, B. K. Choi, I. Jang, S. Ulstrup, S. Kang, T. Thi Ly, S. Kim, Y. H. Choi, C. Jozwiak, A. Bostwick, E. Rotenberg, J. G. Park, R. Sankar, K. S. Kim, J. Kim and Y. J. Chang, *Nano Lett.*, 2018, **18**, 5432–5438.

6 I. Jang, G. Duvjir, B. K. Choi, J. Kim, Y. J. Chang and K. S. Kim, *Phys. Rev. B*, 2019, **99**, 014106.

7 S. Das, S. Senapati, G. K. Pradhan, S. Varadharajanperumal and R. Naik, *ACS Appl. Nano Mater.*, 2023, **6**, 5298–5312.

8 S. R. Das, J. Kwon, A. Prakash, C. J. Delker, S. Das and D. B. Janes, *Appl. Phys. Lett.*, 2015, **106**, 083507.

9 J. Yao and G. Yang, *Nanoscale*, 2020, **12**, 454–476.

10 X. Yu, P. Yu, D. Wu, B. Singh, Q. Zeng, H. Lin, W. Zhou, J. Lin, K. Suenaga, Z. Liu and Q. J. Wang, *Nat. Commun.*, 2018, **9**, 1–9.

11 J. Xia, X. Huang, L. Z. Liu, M. Wang, L. Wang, B. Huang, D. D. Zhu, J. J. Li, C. Z. Gu and X. M. Meng, *Nanoscale*, 2014, **6**, 8949–8955.

12 J. Y. Wu, Y. T. Chun, S. Li, T. Zhang, J. Wang, P. K. Shrestha and D. Chu, *Adv. Mater.*, 2018, **30**, 1705880.

13 D. Zhang, Y. Sun, P. Li and Y. Zhang, *ACS Appl. Mater. Interfaces*, 2016, **8**, 14142–14149.

14 D. Zhang, Y. Cao, P. Li, J. Wu and X. Zong, *Sens. Actuators, B*, 2018, **265**, 529–538.

15 W. Zheng, Y. Xu, L. Zheng, C. Yang, N. Pinna, X. Liu and J. Zhang, *Adv. Funct. Mater.*, 2020, **30**, 2000435.

16 R. M. Alsharabi, J. Singh, P. S. Saxena and A. Srivastava, *Luminescence*, 2024, **39**, e4896.

17 X. Xie, S. Li, J. Chen, J. Ding, J. He, Z. Liu, J. T. Wang and Y. Liu, *ACS Appl. Mater. Interfaces*, 2024, 53220–53230.

18 V. Kumar, G. Afreen, S. R. Ka, P. Mane, B. Chakraborty, C. S. Rout and K. V. Adarsh, *J. Phys. Chem. C*, 2023, **127**, 18485–18493.

19 S. Das and N. Mohapatra, *J. Phys.:Conf. Ser.*, 2023, **2518**, 012010.

20 X. Li, Y. Zhang, Y. Zhao, X. Shi, T. Feng and K. Zhang, *Ann. Phys.*, 2021, **533**, 2100230.

21 L. Li, X. Li, Y. Zhao, J. Feng, C. Zhang, Y. Shi, Y. Ge and Y. Zhang, *Nanotechnology*, 2021, **33**, 065203.

22 D. Sahoo and R. Naik, *J. Non-Cryst. Solids*, 2022, **597**, 121934.

23 C. Shang, Y. Zhang, G. Wang, J. Sun, Y. Cheng, Y. B. Zhang, B. Yao, B. Fu and J. Li, *J. Alloys Compd.*, 2022, **918**, 165580.

24 M. R. El-Aassar, R. K. Sendi, A. Atta, N. Al-Harbi, M. Rabia and M. M. Abdelhamied, *Opt. Quantum Electron.*, 2023, **55**, 1–17.

25 J. Zhang, H. Chen, M. Zhang, H. Yuan, J. Yin, J. Wang and P. Yan, *ICOCN*, 2019, 1–4.

26 P. Priyadarshini, A. Parida, D. Alagarasan, R. Ganesan and R. Naik, *J. Appl. Phys.*, 2023, **133**, 063104.

27 S. N. M. Tawil, C. A. Norhidayah, N. Sarip, S. A. Kamaruddin, A. R. Nurulfadzilah, A. Miskon and M. Z. Sahdan, *J. Nanosci. Nanotechnol.*, 2015, **15**, 9212–9216.

28 D. Kufer and G. Konstantatos, *ACS Photonics*, 2016, **3**, 2197–2210.

29 L. Cheng, C. Yuan, S. Shen, X. Yi, H. Gong, K. Yang and Z. Liu, *ACS Nano*, 2015, **9**, 11090–11101.

30 D. Sarkar, X. Xie, J. Kang, H. Zhang, W. Liu, J. Navarrete, M. Moskovits and K. Banerjee, *Nano Lett.*, 2015, **15**, 2852–2862.

31 C. N. M. Ouma, S. Singh, K. O. Obodo, G. O. Amolo and A. H. Romero, *Phys. Chem. Chem. Phys.*, 2017, **19**, 25555–25563.

32 D. Dash and D. Sahu, *IOP Conf. Ser.:Mater. Sci. Eng.*, 2022, **1219**, 012037.

33 K. Safeen, A. Safeen, D. Arif, W. H. Shah, A. Ali, G. Ali, F. Hussain, N. Imran, A. Ullah Shah, A. Alataway, A. Z. Dewidar, H. O. Elansary, M. Al-Yafrsi and K. S. Ahmad, *Water*, 2023, **15**, 1470.

34 M. J. I. Khan, Z. Kanwal, N. Usmani, P. Akhtar and S. Hussain, *Mater. Res. Express*, 2019, **6**, 115916.

35 W. Wang, X. Zhang, W. Wang, Y. Xue, D. Sheng, M. Xie and A. Xie, *Nanotechnology*, 2024, **35**, 305704.

36 J. Yang, M. Gao, L. Yang, Y. Zhang, J. Lang, D. Wang, Y. Wang, H. Liu and H. Fan, *Appl. Surf. Sci.*, 2008, **255**, 2646–2650.

37 M. Yang, X. Cheng, Y. Li, Y. Ren, M. Liu and Z. Qi, *Appl. Phys. Lett.*, 2017, **110**, 093108.

38 C. Huang, S. Wu, A. M. Sanchez, J. J. P. Peters, R. Beanland, J. S. Ross, P. Rivera, W. Yao, D. H. Cobden and X. Xu, *Nat. Mater.*, 2014, **13**, 1096–1101.

39 F. Ming, H. Liang, Y. Lei, W. Zhang and H. N. Alshareef, *Nano Energy*, 2018, **53**, 11–16.

40 S. Ratha, P. Bankar, A. S. Gangan, M. A. More, D. J. Late, J. N. Behera, B. Chakraborty and C. S. Rout, *J. Phys. Chem. Solids*, 2019, **128**, 384–390.

41 W. Yu, J. Li, T. S. Herng, Z. Wang, X. Zhao, X. Chi, W. Fu, I. Abdelwahab, J. Zhou, J. Dan, Z. Chen, Z. Chen, Z. Li, J. Lu, S. J. Pennycook, Y. P. Feng, J. Ding and K. P. Loh, *Adv. Mater.*, 2019, **31**, 1903779.

42 L. Najafi, R. Oropesa-Nunez, S. Bellani, B. Martin-Garcia, L. Pasquale, M. Serri, F. Drago, J. Luxa, Z. Sofer, D. Sedmidubsky, R. Brescia, S. Lauciello, M. I. Zappia, D. V. Shinde, L. Manna and F. Bonaccorso, *ACS Nano*, 2022, **16**, 351–367.

43 P. Makuła, M. Pacia and W. Macyk, *J. Phys. Chem. Lett.*, 2018, **9**, 6814–6817.

44 S. Landi, I. R. Segundo, E. Freitas, M. Vasilevskiy, J. Carneiro and C. J. Tavares, *Solid State Commun.*, 2022, **341**, 114573.

45 X. Y. Yi, C. Y. Ma, F. Yuan, N. Wang, F. W. Qin, B. C. Hu and Q. Y. Zhang, *Thin Solid Films*, 2017, **636**, 339–345.

46 A. Khan, M. Shkir, M. A. Manthrammel, V. Ganesh, I. S. Yahia, M. Ahmed, A. M. El-Toni, A. Aldalbahi, H. Ghaithan and S. AlFaify, *Ceram. Int.*, 2019, **45**, 10133–10141.

47 A. Parida, A. Devarajan and R. Naik, *Dalton Trans.*, 2025, **54**, 1111–1126.

48 P. Chaiworn, A. Kambut, P. Pluengphon, E. Wongrat, C. Wichasilp and A. Tubtimtae, *Semicond. Sci. Technol.*, 2024, **39**, 115012.

49 A. Parida, S. Senapati, S. Samal, S. Bisoyi and R. Naik, *ACS Appl. Nano Mater.*, 2023, **6**, 11230–11241.

50 M. Shkir, Z. R. Khan, A. Khan, K. V. Chandekar, M. A. Sayed and S. AlFaify, *Ceram. Int.*, 2022, **48**, 14550–14559.

51 P. Suttiyarak and A. Tubtimtae, *Appl. Surf. Sci.*, 2020, **527**, 146835.

52 C. Chainiwetwattana, E. Wongrat and A. Tubtimtae, *Opt. Mater.*, 2023, **138**, 113640.

53 T. G. Ulusoy Ghobadi, B. Patil, F. Karadas, A. K. Okyay and E. Yilmaz, *ACS Omega*, 2017, **2**, 8319–8329.

54 X. Ren, X. Jing, L. Liu, L. Guo, M. Zhang and Y. Li, *RSC Adv.*, 2014, **4**, 53987–53992.

55 H. Yang, T. Yang, H. Zhu, M. Zhang and M. Du, *Chem. Lett.*, 2016, **45**, 69–71.

56 P. Vijayakumar, R. Govindaraj, N. Santhosh, M. S. Pandian, A. Pandikumar and P. Ramasamy, *J. Mater. Sci.*, 2018, **53**, 4444–4455.

57 P. C. Kumar, A. Mohapatra, S. Senapati, M. Pradhan and R. Naik, *FlatChem*, 2023, **42**, 100580.

58 A. Priyadharshini and S. Kalainathan, *J. Mater. Sci.:Mater. Electron.*, 2017, **28**, 7401–7412.

59 R. Bairy, A. Jayarama and M. S. Murari, *Appl. Phys. A:Mater. Sci. Process.*, 2020, **126**, 1–15.

60 M. Parishani, M. Nadafan and S. Akbarpoor, *RSC Adv.*, 2024, **14**, 27741–27748.

61 K. John U and S. Mathew, *Appl. Phys. A:Mater. Sci. Process.*, 2022, **128**, 1–11.

62 F. A. Samad, A. Mahmoud, M. S. Abdel-Wahab, W. Z. Tawfik, R. Zakaria, V. R. Soma, T. Mohamed and T. Mohamed, *J. Opt. Soc. Am. B*, 2022, **39**, 1388–1399.

63 V. Pradeep Kumar, C. Pradeep, M. M. Rajsha, K. P. M. Rishad, P. Radhakrishnan and A. Mujeeb, *Opt. Mater.*, 2023, **142**, 114063.